Revisiting the thermoelectric transport of monolayer InP_3 with full *ab initio* calculations

Hanwen Chen,[1] Chunhui Li,[2] Lei Shan,[1,3,*] and Long Cheng[1,†]

[1]*School of Physics and Electronics, Hunan University, Changsha 410082, China*

[2]*School of Computational Science and Electronics, Hunan Institute of Engineering, Xiangtan 411104, China*

[3]*National Engineering Research Center of RVC, Hunan University, Changsha 410082, China*

(Received 26 January 2024; revised 13 May 2024; accepted 14 May 2024; published 4 June 2024)

Thermoelectric materials facilitate the mutual conversion of thermal energy and electric energy, representing environmentally friendly candidates for power generation. Consequently, there is significant interest in two-dimensional materials due to their potential for achieving superior thermoelectric performance when compared to their bulk counterparts. However, theoretical overestimations are prevalent for many of them, which originates from the fact that most theoretical studies have utilized a constant relaxation time within the framework of a single-mode deformation potential theory (DPT). In this work, we take monolayer InP_3 as an example to systematically revisit its thermoelectric transport by using parameter-free *ab initio* calculations combined with the Boltzmann transport equation. It is found that the scatterings from longitudinal acoustic phonons to charge carriers are not the most influential ones in monolayer InP_3, manifesting that the scattering rates are significantly underestimated within the crude approximation of single-mode DPT. By considering the state-dependent electron-phonon scattering rates, the monolayer InP_3 is found to have room-temperature maximum ZT values of 0.37 and 0.18 for n- and p-type doping, respectively, which are one order of magnitude smaller than those predicted using a constant scattering rate from single-mode DPT. We demonstrate that conventional methods like single-mode DPT do not adequately describe the thermoelectric properties of monolayer InP_3. To calculate the thermoelectric transport of monolayer InP_3 properly, one needs to consider the scatterings from all phonons. We not only uncover the underlying mechanisms governing thermoelectric transport, but also offer a paradigm approach to accurately predict the thermoelectric transport with less computation cost.

DOI: 10.1103/PhysRevB.109.224103

I. INTRODUCTION

Thermoelectric materials possess the capability to directly convert waste heat to electricity, offering a promising avenue for green energy conversion [1–3]. The performance of a thermoelectric material is determined by the dimensionless figure of merit $ZT = S^2\sigma T/(\kappa_e + \kappa_l)$, where S is the Seebeck coefficient, σ is the electrical conductivity, T is the absolute temperature, κ_e is the electronic thermal conductivity, and κ_l is the lattice thermal conductivity. Theoretical studies show that the energy conversion efficiency of thermoelectric materials becomes comparable to that of traditional power generation technologies, provided the corresponding ZT values can be increased to 3.0 [4–6]. However, due to intricate interrelations among those transport coefficients, it is challenging to enhance thermoelectric performance. Over the past decades, several novel concepts and strategies have been proposed to improve thermoelectric performance, e.g., band engineering to optimize the electrical transport [7], introducing anharmonicity to suppress the lattice thermal transport [8,9], etc. Thanks to those endeavors, ZT values exceeding 2.0 have been achieved in several materials [10–12].

Of all the strategies, low dimensionalization is considered one of the most promising methods to achieve high ZT values. This is attributed to the quantum confinement effect arising from their two-dimensional (2D) nature, which can partially decouple the relations between S and σ while suppressing κ_l [13,14]. On that foundation, considerable research efforts have been devoted to investigating the thermoelectric transport of 2D materials. For instance, experimentally, Lee *et al.* found that the electrical conductivity increases, while thermal conductivity decreases, with decreasing thickness in SnS_2. This results in a room-temperature ZT value of 0.13 for 2D SnS_2, which is 1000 times greater than the corresponding bulk material [15]. Zhang *et al.* found that with the reduced dimensionality, the power factor of superlattice $SrTi_{1-x}Nb_xO_3$ is doubled compared with the corresponding bulk [16]. However, the thermoelectric performance of 2D materials experimentally realized is still much lower (typically, the ZT value is < 0.5) than those of conventional bulk thermoelectric materials [17]. On the theoretical side, many 2D materials have been predicted to have large ZT values [18,19]. For example, recent research indicates that monolayer InP_3 exhibits a combination of poor lattice thermal transport and high electrical transport [20–23], yielding a notable maximum ZT value of 4.6 at 500 K [24]. Surprisingly, despite that numerous new 2D materials are predicted to possess high ZT values, none of them have been realized in experiments. The

*Corresponding author: leishan@hnu.edu.cn

†Corresponding author: lcheng@hnu.edu.cn

significant difference motivates us to reexamine the methods employed in the theoretical calculations.

The theoretical methods employed in previous research can be summarized as follows:

(1) The κ_l is calculated through parameter-free *ab initio* calculations by considering three phonon-phonon scatterings. The approach, although computationally expensive, has become more affordable in recent years due to the significant advancements in computational power and the development of algorithms [25–30].

(2) The electrical transport is calculated by solving the Boltzmann transport equation with constant relaxation time τ approximation [31,32], where the constant τ is determined using single-mode deformation potential theory (DPT) [33,34]. The computational cost for the electrical transport is relatively small for this method. Based on the above method, many 2D materials have been predicted to be excellent thermoelectrics with *ZT* values well above 2.0 [17,19,35].

In most previous theoretical research, lattice thermal transport has been studied at great computational expense, while electrical transport is obtained using simple approximations with low computational cost. More precisely, the single-mode DPT only considers the scattering from long-range longitudinal acoustic (LA) phonons to electrons and assumes an isotropic electron-phonon coupling strength. The simplifications may yield significantly inaccurate predictions. For instance, there are many different phonons in a material, e.g., optical phonons, transverse acoustic phonons, out-of-plane phonons, etc. All those phonons can scatter with electrons, and, in many materials, phonons other than long-range LA phonons scatter more frequently with electrons [36–38]. The inclusion of all phonons scattering with charge carriers has shown significant influence in thermal transport in metallic systems, electrical transport in both bulk and two-dimensional materials, thermoelectric transport in silicon-germanium alloys, and optical absorption in boron phosphide [39–45]. Therefore, to accurately predict thermoelectric transport, one has to consider the scattering from all phonons with electrons. Moreover, the conventional density functional theory (DFT) usually underestimates the band gap; to predict the thermoelectric transport properties more accurately, one needs to start with the electronic energies from more precise methods, i.e., HSE and GW approximations [43,46].

In this paper, we take monolayer InP_3 as an example to revisit its thermoelectric transport by using parameter-free *ab initio* calculations. We provide some tricks to significantly reduce the computational cost in lattice thermal transport simulations, which can be extended to other systems. Our findings reveal that monolayer InP_3 has one of the smallest κ_l in 2D materials, which arises from the low group velocity and large phonon-phonon scattering phase space. The conduction band minimum (CBM) is located at the Γ point with a sharp valley, resulting in small "density of scatterings" [37] and consequently high electron mobility, whereas the highest valence band has multiple valleys, leading to large density of scatterings and thus low hole mobility. By decomposing the contributions from different phonon modes, we find that electrons (holes) scatter more heavily with optical phonons than LA phonons. Our results reveal that, to accurately predict the thermoelectric transport of monolayer InP_3, it is required to consider the scatterings from all phonons. Furthermore, our calculations show the maximum *ZT* value is 0.37 at 300 K. This finding suggests that the conventional theoretical methods in previous research substantially overestimate the thermoelectric properties.

II. METHODS

A. Thermal transport

The $4 \times 4 \times 1$ supercell and $4 \times 4 \times 1$ **q** grids are chosen to calculate the second-order force constants by using the supercell method, as implemented in the VASP [47–49] and PHONOPY [27,50] packages. The box along the out-of-plane direction is set as 24 Å to avoid interactions between images. The relative root mean square (RRMS) of the second-order force constants is then used to determine the cutoff radius in the calculation of third-order force constants (see Appendix A). The $4 \times 4 \times 1$ supercell and Γ point are chosen to calculate the third-order force constants. The determined cutoff radius is 7.8 Å, which corresponds to the seventh-nearest neighbors. The lattice thermal transport is calculated by solving the linearized phonon Boltzmann transport equation iteratively [51] as implemented in the PHOEBE package [30]. The $75 \times 75 \times 1$ **q** grids are employed to get converged lattice thermal conductivity (see the convergence test of κ_l with the number of **q** grids in Appendix B).

B. Charge carrier transport

The QUANTUM ESPRESSO package [52] with the SG15 optimized norm-conserving Vanderbilt (ONCV) pseudopotentials [53,54] and the Perdew-Burke-Ernzerhof (PBE) [55] exchange-correlation functional are employed in the calculation of electrical transport. The kinetic energy cutoffs for wave functions and charge density are set to 60 and 240 Ry, respectively. The atomic coordinates are optimized using a 24×24 **k** mesh until the magnitude of the force acting on each atom becomes less than 0.0001 Ry/bohr. To predict the charge carrier transport and the thermoelectric transport coefficients more accurately, the electronic energies are calculated by using the Heyd-Scuseria-Ernzerhof (HSE06) screened hybrid functional [56] (the results from standard PBE are also calculated for comparison). It is found that the change in band gap would not affect the electron-phonon scattering rates (see Appendix C). We have chosen one *s* orbital and three *p* orbitals for both In and P atoms in constructing the Wannier projections.

The charge carrier mobility is calculated as [38]

$$\mu_{\alpha\beta} = e\frac{\sum_i \int_{\mathrm{BZ}} \tau_{i\mathbf{k}} v_{i\mathbf{k},\alpha} v_{i\mathbf{k},\beta} \left|\frac{\partial f_{i\mathbf{k}}}{\partial E_{i\mathbf{k}}}\right| d\mathbf{k}}{\sum_i \int_{\mathrm{BZ}} f_{i\mathbf{k}} d\mathbf{k}}, \tag{1}$$

where α and β represent Cartesian directions, e is the unit charge, $\tau_{i\mathbf{k}}$ is the relaxation time of the electronic state $i\mathbf{k}$ marked by the band index i and the wave vector $\mathbf{k}$, v is the electronic band velocity, f is the Fermi-Dirac distribution at equilibrium, and E is the electronic energy. The summation is over conduction bands for electrons and valence bands for holes. The scattering rates $1/\tau_{i\mathbf{k}}$ from all phonons can be

calculated as [57]

$$\frac{1}{\tau_{i\mathbf{k}}} = \sum_{\lambda,j}\int_{\mathrm{BZ}}\frac{2\pi}{\hbar}\frac{d\mathbf{q}}{\Omega_{\mathrm{BZ}}}\{|g(i\mathbf{k},\, j\mathbf{k}',\, \lambda\mathbf{q})|^2 \times [(f_{j\mathbf{k}'}+n_{\lambda\mathbf{q}})\delta(E_{i\mathbf{k}}-E_{j\mathbf{k}'}+\hbar\omega_{\lambda\mathbf{q}})\delta_{\mathbf{k}+\mathbf{q},\mathbf{k}'+\mathbf{G}} +(1+n_{\lambda\mathbf{q}}-f_{j\mathbf{k}'})\delta(E_{i\mathbf{k}}-E_{j\mathbf{k}'}-\hbar\omega_{\lambda\mathbf{q}})\delta_{\mathbf{k}-\mathbf{q},\mathbf{k}'+\mathbf{G}}]\}, \tag{2}$$

where $g(i\mathbf{k},\, j\mathbf{k}',\, \lambda\mathbf{q})$ is the electron-phonon coupling strength. n is the Bose-Einstein distribution, $\omega_{\lambda\mathbf{q}}$ is the phonon frequency with phonon band index λ and wave vector $\mathbf{q}$. Ω_{BZ} is the volume of the first Brillouin zone (BZ). $\mathbf{G}$ is the reciprocal lattice vector. The two δ functions represent the energy conservation law and the quasimomentum conservation law.

To obtain the charge carrier mobility, we first employ density functional perturbation theory (DFPT) [58,59] to calculate g on 9×9 $\mathbf{k}$ and 9×9 $\mathbf{q}$ grids. Then g of 240×240 $\mathbf{k}$ (to reduce the computation cost, we have used the symmetry of the lattice, and thus only the 4921 irreducible $\mathbf{k}$ points need to be considered) and 240×240 $\mathbf{q}$ grids are obtained using the interpolation approach [60] as implemented in the EPW package [61]. To properly account for the 2D Fröhlich scattering, we have implemented the 2D Fröhlich model by Sohier *et al.* [62] into our in-house EPW package, which enables more accurate calculation of the intrinsic charge carrier transport for 2D polar semiconductors.

C. Thermoelectric transport

The thermoelectric transport coefficients S, σ, and κ_{e} are calculated as [63]

$$\sigma_{\alpha\beta}(T,E_f) = \frac{1}{A_{\mathrm{area}}}\sum_i\int_{\mathrm{BZ}} -e^2 v_{i\mathbf{k},\alpha}v_{i\mathbf{k},\beta}\tau_{i\mathbf{k}}\frac{\partial f_{i\mathbf{k}}}{\partial E_{i\mathbf{k}}}d\mathbf{k}, \tag{3a}$$

$$S_{\alpha\beta}(T,E_f) = -\frac{1}{eT}\frac{\sum_i\int_{\mathrm{BZ}}(E_{i\mathbf{k}}-E_f)v_{i\mathbf{k},\alpha}v_{i\mathbf{k},\beta}\tau_{i\mathbf{k}}\frac{\partial f_{i\mathbf{k}}}{\partial E_{i\mathbf{k}}}d\mathbf{k}}{\sum_i\int_{\mathrm{BZ}}v_{i\mathbf{k},\alpha}v_{i\mathbf{k},\beta}\tau_{i\mathbf{k}}\frac{\partial f_{i\mathbf{k}}}{\partial E_{i\mathbf{k}}}d\mathbf{k}}, \tag{3b}$$

$$\kappa_{e,\alpha\beta}(T,E_f) = -TS^2_{\alpha\beta}(T,E_f)\sigma_{\alpha\beta}(T,E_f) - \frac{1}{TA_{\mathrm{area}}} \times\sum_i\int_{\mathrm{BZ}}(E_{i\mathbf{k}}-E_f)^2 v_{i\mathbf{k},\alpha}v_{i\mathbf{k},\beta}\tau_{i\mathbf{k}}\frac{\partial f_{i\mathbf{k}}}{\partial E_{i\mathbf{k}}}d\mathbf{k}, \tag{3c}$$

where A_{area} is the surface area of the primitive cell. E_f is the chemical potential that corresponds to the carrier concentration. The correspondence between the carrier concentration and the Fermi level is

$$n_{\mathrm{electrons}} = \frac{1}{A_{\mathrm{area}}}\sum_i\int_{\mathrm{BZ}}\frac{1}{e^{(E_{i\mathbf{k}}-E_f)}+1}d\mathbf{k}, \tag{4}$$

for electrons, and

$$p_{\mathrm{holes}} = \frac{1}{A_{\mathrm{area}}}\sum_i\int_{\mathrm{BZ}}\frac{1}{e^{(E_f-E_{i\mathbf{k}})}+1}d\mathbf{k}, \tag{5}$$

for holes. The summation is over conduction bands for electrons and valence bands for holes.

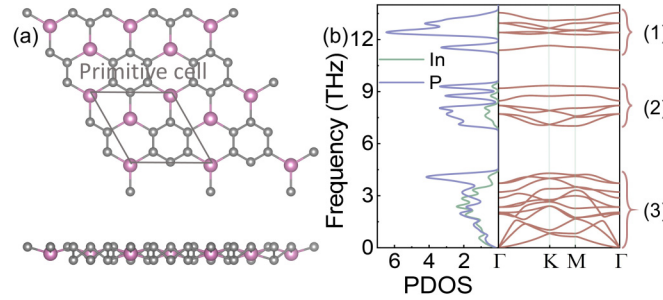

FIG. 1. (a) Lattice structure of monolayer InP_3. Views from above (top) and from the side (bottom) are shown. The primitive cell is marked by the dark gray rhombus. The In and P atoms are denoted by the pink and light gray balls, respectively. (b) Phonon band structure and atom projected phonon density of states (PDOS) of monolayer InP_3. Contributions from In and P atoms are represented by green and purple lines, respectively. The 24 phonon modes can be classified into three classes. The structures are shown using the VESTA code [64].

The ZT value is then calculated as

$$ZT_{\alpha\beta}(T,E_f) = \frac{S^2_{\alpha\beta}(T,E_f)\sigma_{\alpha\beta}(T,E_f)}{\kappa_{e,\alpha\beta}(T,E_f)+\kappa_l}T. \tag{6}$$

III. RESULTS AND DISCUSSION

A. Thermal transport

The optimized lattice structure of monolayer InP_3 is illustrated in Fig. 1(a). Its crystal structure belongs to the space group $P\bar{3}m1$. The primitive cell is marked by the gray rhombus containing six P atoms and two In atoms. Every six P atoms form a distorted hexagon, and these P hexagons are connected by the In atoms. The In atoms also form a larger hexagon. The lattice constant is 7.52 Å and the thickness is 4.82 Å. Note that the thickness is defined as the summation of the buckling thickness 1.22 Å (the distance between the two outer P atomic planes) and the van der Waals radius of the P atom, 1.8 Å. The calculated structural properties are in good agreement with the previous study [20,21,24].

Based on the optimized lattice structure, we calculated the harmonic force constants and obtained the phonon band structure as shown in Fig. 1(b). It is found that there is no imaginary frequency, confirming its stability. The 24 phonon bands can be classified into 3 classes: (1) the six highest optical phonon bands (in the range 11–14 THz), (2) the middle six optical phonon bands (in the range 7–10 THz), and (3) the nine lowest optical phonon bands and the three acoustic phonon bands (in the range 0–5 THz). Classes 1 and 2 are relatively flat, indicating small phonon velocity, which is beneficial to small lattice thermal conductivity. On the other hand, the class 3 phonons are much more dispersive. Interestingly, those 12 phonon bands intertwine with each other, which is similar to the rattling modes in some host-guest systems, i.e., clathrates and skutterudites [65–68]. This feature gives rise to higher anharmonicity and phonon-phonon scatterings (shown later), leading to small lattice thermal conductivity. We have also plotted the atom projected phonon density of states (PDOS) to illustrate the contributions of atoms to the phonon modes. It

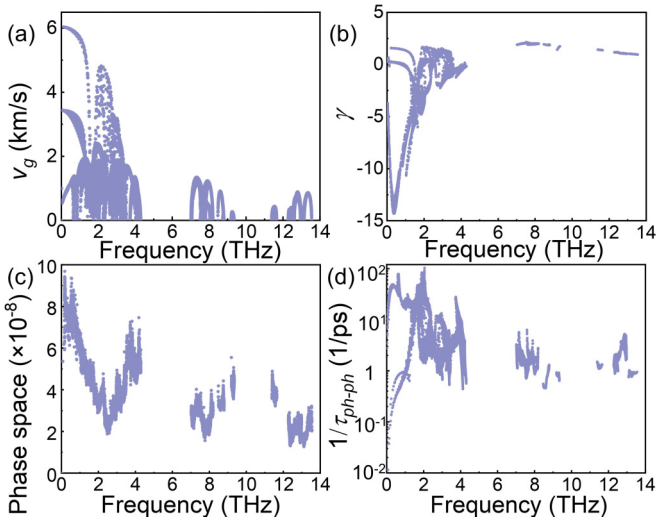

FIG. 2. Calculated (a) phonon group velocity v_g, (b) Grüneisen parameter γ, (c) phonon-phonon scattering phase space, and (d) phonon-phonon scattering rates $1/\tau_{\mathrm{ph-ph}}$.

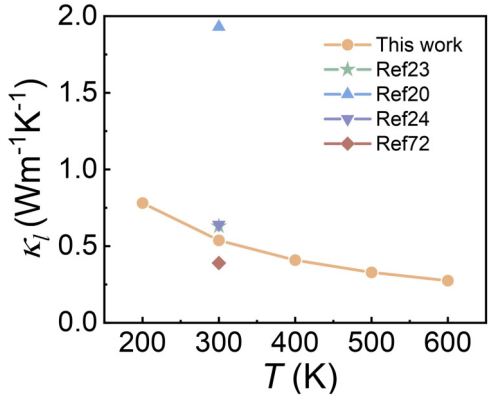

FIG. 3. Calculated lattice thermal conductivity κ_l as a function of temperature. The room-temperature κ_l is 0.54 W m^{-1} K^{-1}, which is among the lowest in 2D materials.

is found that the six highest optical phonon modes are purely due to the vibrations of P atoms, which corresponds to the variation of the P hexagons.

Figure 2(a) shows the calculated phonon group velocity v_g. Indeed, the v_g of the 12 highest optical phonon modes are small (<1 km/s), and the v_g of the acoustic phonons are larger. However, the v_g of the acoustic phonons (6 km/s) are much smaller than that of graphene (22 km/s) [69], and also smaller than that of some common 2D materials, i.e., black phosphorene (7.7 km/s) [70] and monolayer MoS_2 (6.4 km/s) [71]. The relatively small v_g is an indication of low κ_l. Moreover, the three-phonon scattering phase space [68] of the class 3 phonons is larger than those of classes 1 and 2 as shown in Fig. 2(c). This is because the scattering process must obey the energy and momentum conservation laws and lots of scattering processes would be prohibited. For instance, the minimum phonon frequency in class 2 is about 6.5 THz, and the maximum phonon frequency in class 1 is 13.5 THz. Therefore, only few phonons can scatter from class 2 to class 1 via absorption, and vice versa via emission. In addition, the absolute Grüneisen parameters are significantly larger for acoustic phonons [see Fig. 2(b)], indicating higher anharmonicity, which would lead to higher scattering strength of acoustic phonons. Consequently, the scattering rates $1/\tau_{\mathrm{ph-ph}}$ of the class 3 phonons are one to two orders of magnitude larger than the class 1 and 2 phonons, as shown in Fig. 2(d). The small v_g and relatively high $1/\tau_{\mathrm{ph-ph}}$ indicates that monolayer InP_3 has low κ_l.

Indeed, monolayer InP_3 has a relatively small κ_l, which is 0.54 W m^{-1} K^{-1} at 300 K, and our results agree well with the previous study [23,24,72]. Note that, for monolayers, the exact value of the conductivity (both electrical and thermal) depends on the thickness. Unless otherwise stated, all the values are with respect to the thickness of 4.82 Å. The small discrepancy originates from the utilization of different supercells in calculating third-order force constants and the minor difference in the definition of thickness. However, values from Sun *et al.* [24], Ouyang *et al.* [23], and Keshri *et al.* [72] and our calculated κ_l are much smaller than that from Ref. [20], which may arise from the use of different exchange correlations in their calculation of κ_l. Nevertheless, the κ_l of monolayer InP_3 is much lower than most common 2D materials. For instance, the room-temperature κ_l of black phosphorene is over 20 W m^{-1} K^{-1} [73], and the κ_l of monolayer MX_2 (M = Mo, W; X = S, Se) is over 50 W m^{-1} K^{-1} [71,74]. The κ_l can be further reduced with increasing temperature (see Fig. 3), since more phonons would be excited and thus phonon-phonon scattering rates would be larger.

B. Electronic structures

Figure 4(a) shows the calculated electronic band structure of monolayer InP_3. The results from HSE and PBE are both shown. Monolayer InP_3 is semiconducting with an indirect band gap, and the band gap is 0.71 eV with PBE and 1.32 eV with HSE. Unless otherwise stated, the transport properties are obtained starting from the electronic energies with HSE. The CBM is located at the Γ point and the average electron effective mass is $0.139m_e$, which is beneficial for small density of scatterings [75]. However, there is a second-lowest CBM at the Γ point, which is assumed to be disadvantageous to high electron mobility because it may introduce extra intervalley scatterings between the two valleys. To make it clearer, we plot the three-dimensional (3D) energy band structures around the Γ point in Fig. 4(b). It is found that the energy difference ΔE between the two valleys is 110 meV. The ΔE is much larger than the largest phonon energy (56 meV). As a consequence, the intervalley scattering would be significantly suppressed due to the energy conservation law. Therefore, we can conclude that monolayer InP_3 has an optimal electronic structure feature for high electron mobility: a steep and deep valley located at the Γ point [75]. This sharp single valley indicates small density of states and thus small Seebeck coefficients, because S is proportional to the density of states.

By contrast, the valence band maximum (VBM) is located at the ΓM line. There are six equivalent valleys due to the sixfold rotational symmetry. Apart from the intravalley scattering, there are intervalley scatterings among different valleys. Moreover, there are six other valleys that are 40 meV

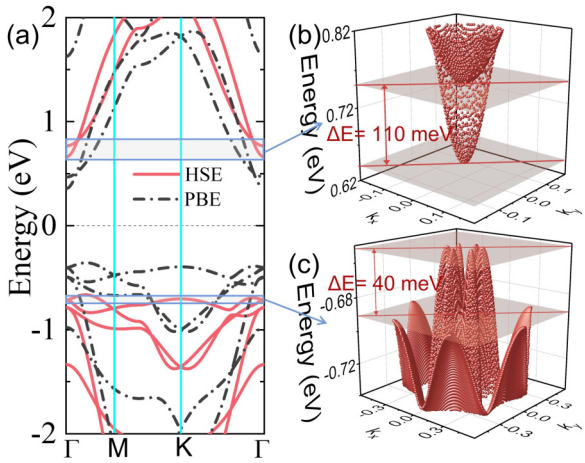

FIG. 4. (a) Calculated electronic band structure of monolayer InP_3 along the high-symmetry lines Γ-M-K-Γ. The band structures from PBE and HSE are denoted by dashed gray lines and solid red lines, respectively. The 3D electronic structure around the (b) conduction band minimum (CBM) and (c) valence band minimum (VBM). The energy difference between the CBM and the second lowest CBM is 110 meV. The energy difference between the VBM and the second-highest VBM is 40 meV. Note that the maximum phonon energy is 56 meV. Therefore, we can conclude that monolayer InP_3 has an optimal electronic structure feature for high electron mobility.

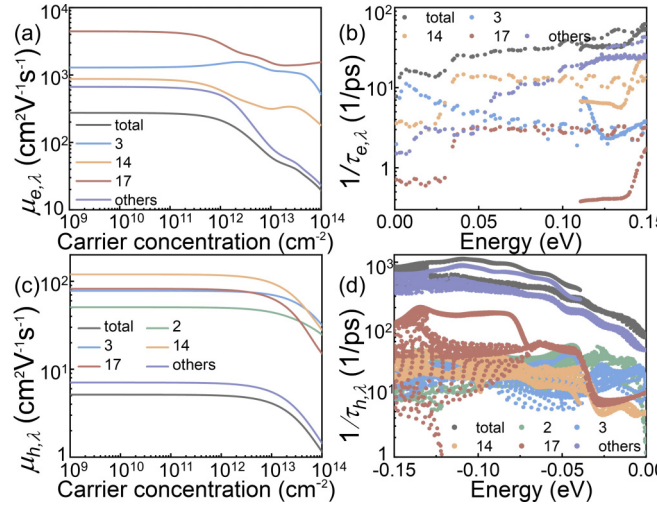

FIG. 5. Calculated mode-resolved (a) electron mobility $\mu_{e,\lambda}$ as a function of carrier concentration and (b) electron-phonon scattering rates $1/\tau_{e,\lambda}$ as a function of electronic energy at 300 K. The CBM has been shifted to 0 eV. Calculated mode-resolved (c) hole mobility $\mu_{h,\lambda}$ as a function of carrier concentration and (d) hole-phonon scattering rates $1/\tau_{h,\lambda}$ as a function of electronic energy at 300 K. The VBM has been shifted to 0 eV. The phonon modes are numbered from 1 to 24 with increasing frequency.

lower than the VBM [see Fig. 4(c)]. The ΔE is within the range of the phonon energy. The K valley is also close to the VBM in energy. In consequence, there are also extra intervalley scatterings from those other eight valleys. Therefore, the electronic structure for holes has 14 valleys, and the holes will have both large intravalley and intervalley scatterings, leading to high density of scatterings and thus a small hole mobility. The multiple valleys render high density of states and are beneficial to large Seebeck coefficients.

C. Charge carrier transport

Figure 5(a) shows the calculated mode-resolved electron mobility $\mu_{e,\lambda}$ of monolayer InP_3 at room temperature. The intrinsic electron mobility μ_e is 275 $cm^2\,V^{-1}\,s^{-1}$. This high μ_e is larger than most 2D semiconductors, i.e., μ_e of all monolayer transition metal dichalcogenides (MX_2) [37,38] and black phosphorene (BP) [76,77]. However, it is about one order of magnitude lower than that predicted by DPT [20,24]. This is because DPT only considers the scatterings from long-range LA phonons to the electronic band edge states. Figure. 5(b) shows the mode-resolved electron-phonon scattering rates ($1/\tau_{e,\lambda}$), where the CBM has been shifted to 0 eV. The total scattering rate (gray dots) is around 30 ps^{-1} within 150 meV to the band edges. As a comparison, DPT predicts a constant scattering rate of 2.5 ps^{-1}. Therefore, the scattering rates are significantly underestimated within the framework of single-mode DPT. Moreover, it is found that $\mu_{e,14}$ (orange line) has the largest contributions to μ_e, followed by $\mu_{e,3}$ (blue line). Nevertheless, all the phonons contribute to total electron mobility. Furthermore, we observe that μ_e (μ_h) from single-mode DPT is anisotropic, which contradicts the symmetry of the hexagonal lattice, whereas μ_e (μ_h) is isotropic in our calculations when the scatterings from all phonons are considered. In addition, the scattering rates have two branches at energies above 0.11 eV, indicating scatterings from the second-lowest CBM start to get involved.

The intrinsic hole mobility μ_h is 5 $cm^2\,V^{-1}\,s^{-1}$ at room temperature, which is indeed much lower than μ_e, resulting from the much higher scattering rates [see Fig. 5(d)]. Moreover, it is found that $\mu_{h,2}$ (green line, contributions from the transverse acoustic phonons) has the largest contributions to μ_h, followed by $\mu_{h,17}$ (red line) and $\mu_{h,3}$ (blue line). Contributions from the LA phonons only account for less than 5% of the total scattering rates. The overall total scattering rate is ∼100–1000 ps^{-1}, while the constant scattering rate for holes from single-mode DPT is about 6 ps^{-1}. Such a large difference indicates the hole scattering rates are much more underestimated compared with electrons. This is also the reason for the higher p-type ZT value than that of the n type from single-mode DPT (see discussions later). In addition, the scattering rates also have three branches at energies lower than 40 meV, indicating the scatterings from the second-highest VBM and K valleys. The huge drop in carrier mobility at 1010 cm^{-2} from $\mu e = 539(\mu h = 5)$ $cm^2V^{-1}s^{-1}$ at 200 K to $\mu e = 72$ $(\mu h = 1)$ $cm^2V^{-1}s^{-1}$ at 600 K is a consequence of the increased electron-phonon scatterings at high temperature.

Figures 6(a) and 6(c) show the calculated $\mu_{e/h}$ at different temperatures. The huge drop in carrier mobility at 10^{10} cm^{-2} from $\mu e = 539(\mu h = 5)$ $cm^2\,V^{-1}\,s^{-1}$ at 200 K to $\mu e = 72(\mu h = 1)$ $cm^2\,V^{-1}\,s^{-1}$ at 600 K is a consequence of the increased electron-phonon scatterings at high temperature. With increasing temperature, more phonons would be excited. Therefore, the phonon-electron and phonon-hole scattering rates would be much higher, as evidenced in Figs. 6(b) and

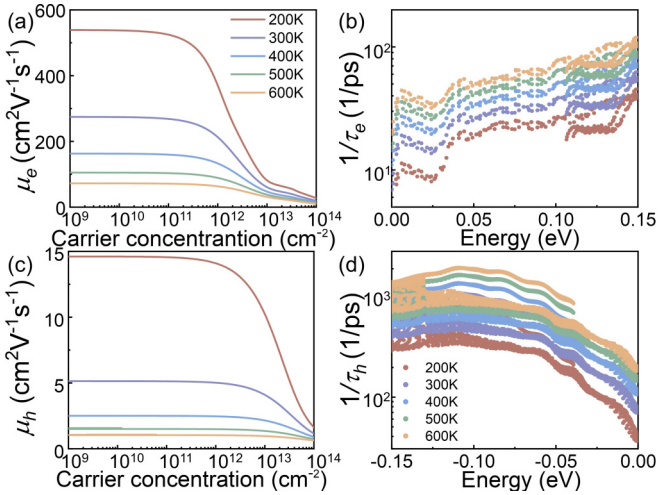

FIG. 6. Calculated total (a) electron mobility μ_e as a function of carrier concentration and (b) electron-phonon scattering rates $1/\tau_e$ as a function of energy at various temperatures. The CBM has been shifted to 0 eV. Calculated total (c) hole mobility μ_h as a function of carrier concentration and (d) hole-phonon scattering rates $1/\tau_h$ as a function of energy at various temperatures. The VBM has been shifted to 0 eV. The red, purple, blue, green, and yellow lines and dots represent 200, 300, 400, 500, and 600 K, respectively.

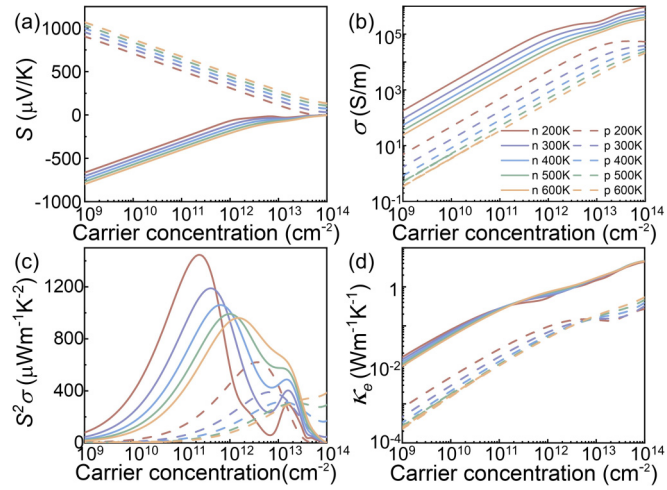

FIG. 7. Calculated (a) Seebeck coefficient S, (b) electrical conductivity σ, (c) power factor (PF) $S^2\sigma$, and (d) electronic thermal conductivity κ_e as a function of carrier concentration at various temperatures. The red, purple, blue, green, and yellow lines represent 200, 300, 400, 500, and 600 K, respectively. The solid and dashed lines represent n-type and p-type dopings, respectively.

6(d). Moreover, we see that $\mu_{e/h}$ is nearly invariable at carrier concentrations below 10^{11} cm^{-2}. This weak dependence is due to the slow changing of the derivative of Fermi-Dirac distributions with carrier concentrations. In addition, $\mu_{e/h}$ decreases rapidly at high carrier concentrations, and as the temperature drops, it decreases faster. This is because the scattering rates are much larger at higher energies as shown in Figs. 6(b) and 6(d). Furthermore, the critical carrier concentration for the rapid drop of $\mu_{e/h}$ is larger at high temperatures. Since the Fermi distribution is flatter at higher temperatures, therefore, both scatterings of high and low energies are modulated by the derivative of the Fermi distribution, delaying the rapid dropping of $\mu_{e/h}$ at high carrier concentrations.

D. Thermoelectric transport

With the fine **k** grids electronic scattering rates, the thermoelectric transport coefficients are calculated using Eq. (3). Figure 7(a) shows the calculated Seebeck coefficients. The absolute $|S|$ decreases with increasing carrier concentration. The $|S|$ is over 200 μV/K at 10^{11} cm^{-2} for both n- and p-type doping, which is comparable to the best thermoelectric, i.e., SnSe [10]. Moreover, the S of p- and n-type doping are asymmetric and the absolute $|S|$ of the former is much larger. In addition, $|S|$ is larger at higher temperatures at certain carrier concentrations. Those features are originated from the band structures and can be explained using the Mott relation:

$$S = \pi k_B^2 T / 3e\varepsilon_f \tag{7}$$

where $\varepsilon_f = n\pi^2/M^*$ is the Fermi level, $M^* = N_v m^*$ is the density-of-states effective mass, m^* is the band effective mass, N_v is the number of equivalent valleys, and n is the carrier concentration. Hence, S is proportional to T, N_v, and m^*, and is inversely proportional to n: $S \propto TN_v m^*/n$. The electronic structure of the lowest conduction band is single valley, while that of the highest valence band has multiple equivalent valleys. Therefore, $|S|$ of p-type doping is higher than that of n-type doping.

At low carrier concentrations, the electrical conductivity has a sharp increase and almost has a linear relation with n. This is reasonable since the scatterings between band edges dominate at low n. However, at high carrier concentrations, there is a small kink around 10^{13} cm^{-2} for n-type and 10^{14} cm^{-2} for p-type carriers. This feature is absent in previous calculations, which assume a constant relaxation time for all the electronic states. The n-type σ is about two orders of magnitude higher than p-type σ at the same carrier concentration. It is because the scattering rates of p-type carriers are much higher, which comes from the large intervalley scatterings. This high scattering rate is inherently arising from the multiple valence band valleys.

The contrary trends of S and σ with n imply there must be a trade-off such that the power factor $S^2\sigma$ can be maximized at an optimal carrier concentration. Indeed, a maximum $S^2\sigma = 1.2$ mW m^{-1} K^{-2} is achieved at $n = 4.0 \times 10^{11}$ cm^{-2} at 300 K for n-type carriers. Our predicted $S^2\sigma$ is about one order of magnitude lower than that assuming a constant relaxation time with single-mode DPT, which is due to the lower σ when all the phonon scatterings are considered. Moreover, there is a second peak for $S^2\sigma$ at high carrier concentration. This is due to the complex scatterings between different electronic states and this feature is also absent in previous calculations, which assume a constant relaxation time for all the electronic states. In addition, $S^2\sigma$ decreases with increasing T within the temperature range under consideration.

Having all the transport coefficients calculated, the ZT value is obtained using Eq. (4). Figure 8 shows the ZT value as a function of carrier concentration at different temperatures. The maximum ZT value is 0.37 for n-type doping with $n = 2.9 \times 10^{11}$ cm^{-2} and 0.18 for p-type doping with

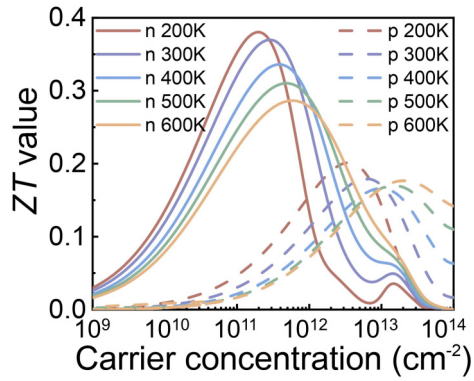

FIG. 8. Calculated ZT value of monolayer InP_3 as a function of carrier concentration at various temperatures. The red, purple, blue, green, and yellow lines represent 200, 300, 400, 500, and 600 K, respectively. The solid and dashed lines represent n-type and p-type dopings, respectively.

$n = 6.5 \times 10^{12}\,\mathrm{cm}^{-2}$ at room temperature. Those values are about an order of magnitude lower than previous predictions, owing to the significant differences in the calculation of electron-phonon scattering rates. More importantly, at certain temperatures, the maximum p-type ZT value is higher than that of the n-type value in the previous study. However, our calculations show a contrary trend. The discrepancy stems from the much more overestimated relaxation time for holes with single-mode DPT. In addition, we would like to mention our calculated ZT values are higher than in Ref. [72] (considered the scattering of all phonons), which is because of the much smaller relaxation time predicted in Ref. [72]. We have shown the detailed comparison in Appendix D. As for the temperature dependence, the maximum ZT value of n-type doping decreases with the increasing T from 0.38 at 200 K to 0.29 at 600 K, while the maximum ZT value of p-type doping shows a weak temperature dependence and is around 0.18 in the whole temperature range. We have plotted the maximum ZT values and the corresponding S, σ, $S^2\sigma$, and κ_e at various temperatures in Appendix E.

For a material with N atoms in the primitive cell, there are $3N$ phonon modes. All phonons can scatter with charge carriers, while single-mode DPT only considers the scattering of charge carriers with long-range LA phonons. In some materials, the contribution of LA phonons to total scattering is not even the largest. For instance, the scattering of polar optical phonons with charge carriers dominates in triangular metal dichalcogenides (T$-MX_2$) [78] and metal monochalcogenides (MX) [38]. Hence, the scattering rates would be significantly underestimated by using single-mode DPT, leading to the overestimated thermoelectric transport properties (ZT value). More importantly, we emphasize that the constant relaxation time predicted by single-mode DPT not only overestimates the ZT values, but may also predict inaccurate or incorrect trends of ZT value with temperatures.

IV. CONCLUSION

To summarize, we have systematically studied the thermoelectric transport properties of monolayer InP_3 by using parameter-free *ab initio* calculations combined with a Boltzmann transport equation. We have offered some tricks to significantly reduce the computational cost in lattice thermal transport calculations. It is found that monolayer InP_3 has a relatively low κ_l, which arises from the small phonon group velocity and the large phonon-phonon scattering phase space. For the charge carrier transport, the scatterings from all phonons are considered. It is found that the scattering from LA phonons is not even the most significant, confirming that the scattering rates are significantly underestimated by using single-mode deformation potential theory. The room-temperature electron mobility is over $200\,\mathrm{cm}^2\,\mathrm{V}^{-1}\,\mathrm{s}^{-1}$ even when the carrier concentration reaches 10^{12} cm^{-2}, while the hole mobility is relatively small. The distinct electron and hole carrier mobilities stem from the electronic band structures. The electrons have a single sharp valley located at the Γ point, resulting in small scattering rates, while holes have multiple valleys, leading to large scattering rates. The thermoelectric transport is then calculated by considering the state-dependent scattering rates. It is found that the room-temperature maximum ZT value of monolayer InP_3 is 0.37 for n- and 0.18 for p-type doping, which is much smaller than those predicted using a constant scattering rate that only considers the scattering between electrons and long-range longitudinal acoustic phonons. Moreover, the maximum ZT value of n type is smaller than that of p type when using single-mode DPT, primarily due to the much more overestimated relaxation time for holes in single-mode DPT. Our study not only accurately predicts the thermoelectric transport of monolayer InP_3, but also uncovers the underlying mechanisms governing the thermoelectric transport and, more importantly, offers a paradigm approach to correctly predicting the thermoelectric transport of 2D thermoelectrics. We demonstrate that our method will be valuable in reexamining the thermoelectric performance of previously predicted excellent thermoelectrics and in predicting the thermoelectric performance of new materials.

The data that support the findings of this study are available from the corresponding author upon reasonable request.

ACKNOWLEDGMENTS

We acknowledge support from the National Key Research and Development Program of Ministry of Science and Technology (Grant No. 2023YFD2100300), the National Natural Science Foundation of China (Grant No. 12104143), Natural Science Foundation of Hunan Province (Grants No. 2022JJ40027 and No. 2022JJ40028), and Fundamental Research Funds for the Central Universities (Grants No. 531118010595 and No. 531118010619).

The authors declare that they have no known competing financial interests or personal relationships that could have appeared to influence the work reported in this paper.

APPENDIX A: RELATIVE ROOT MEAN SQUARE OF SECOND-ORDER FORCE CONSTANTS

To reduce the computational cost in the third-order force constants calculation, we have used the root mean square of the second-order force constants (RMS) [79,80] to determine

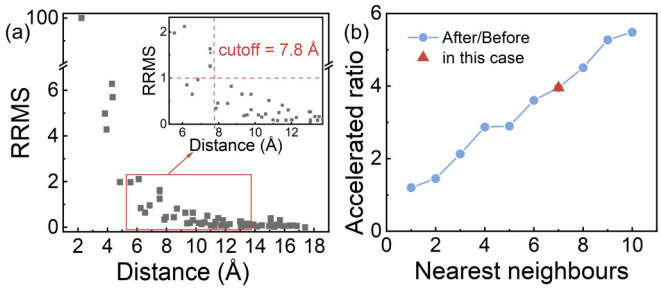

FIG. 9. (a) Calculated relative root mean square of the second-order force constants (RRMS) as a function of atomic distance. It is found that a cutoff radius of 7.8 Å is needed to get converged results, which corresponds to the seventh-nearest neighbors to be considered in the calculation of third-order force constants. (b) The accelerated ratio with the interactions considered in the calculation of third-order force constants.

the cutoff radius:

$$\mathrm{RMS}[\Phi(jl, j'l')] = \frac{1}{3}\sqrt{\sum_{\alpha,\beta}[\Phi_{\alpha\beta}(jl, j'l')]^2}, \tag{A1}$$

where $\Phi_{\alpha\beta}(jl, j'l')$ is the second-order force constant matrix element, which represents the force along the α direction felt by atom j in the lth unit cell due to the displacement of atom j' in the l'th unit cell along the β direction. However, the magnitude of RMS is somewhat arbitrary and differs a lot for different materials. To resolve this issue, we have used the magnitude of relative RMS (RRMS) to determine the cutoff radius:

$$r_{\mathrm{RRMS}}[\Phi(jl, j'l')] = \frac{r_{\mathrm{RMS}}[\Phi(jl, j'l')]}{\{r_{\mathrm{RMS}}[\Phi(jl, j'l')]\}_{\max}}, \tag{A2}$$

where all the RMS values are normalized by the maximum RMS. We have chosen a criterion smaller than 0.01 to determine the cutoff radius. Figure 9 shows the RRMS of monolayer InP_3 with atomic distances. The cutoff radius is 7.8 Å, corresponding to seventh-nearest neighbors. Hence, the total number of cases to be calculated is 548. Considering 12 cases are identical, we only need to do calculations for 537 different cases. We have also implemented the accelerating method proposed by Qin and Hu [80]. The accelerated ratio

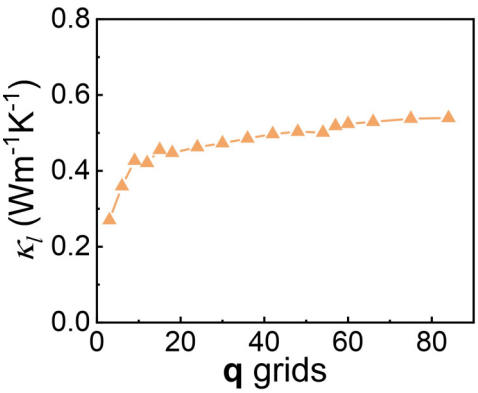

FIG. 10. The effect of the number of **q** grids on lattice thermal conductivity κ_l.

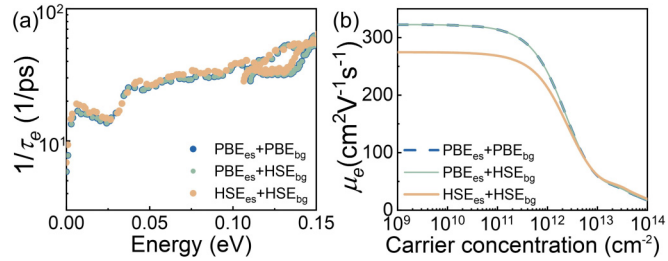

FIG. 11. Calculated room-temperature (a) electron-phonon scattering rates and (b) electron mobility.

is shown in Fig. 9(b). It is found that the computational cost is reduced by 75% in our case. The scripts for decreasing the computational cost are available from the corresponding author.

APPENDIX B: CONVERGENCE TEST OF κ_l WITH NUMBER OF q GRIDS

As mentioned in Sec. II A, sufficiently large **q** grids are needed to get a converged lattice thermal transport property. Figure 10 displays the κ_l with the number of **q** grids. It is found that a $75 \times 75 \times 1$ **q** grid is needed to get converged κ_l. This corresponds to 5625 **q** points in the calculation.

APPENDIX C: EFFECTS OF ELECTRONIC STRUCTURES AND BAND GAPS ON THE ELECTRON-PHONON SCATTERING RATES, CHARGE CARRIER MOBILITY, AND THERMOELECTRIC TRANSPORT COEFFICIENTS

To characterize the influence of electronic structures and band gap on the thermoelectric transport coefficients, we have applied three different methods to study the electron-phonon scattering rates, electron mobility, and thermoelectric transport coefficients of monolayer InP_3: (1) start from the PBE-calculated band structures and band gap (denoted as PBEes+PBEbg); (2) start from the PBE-calculated band

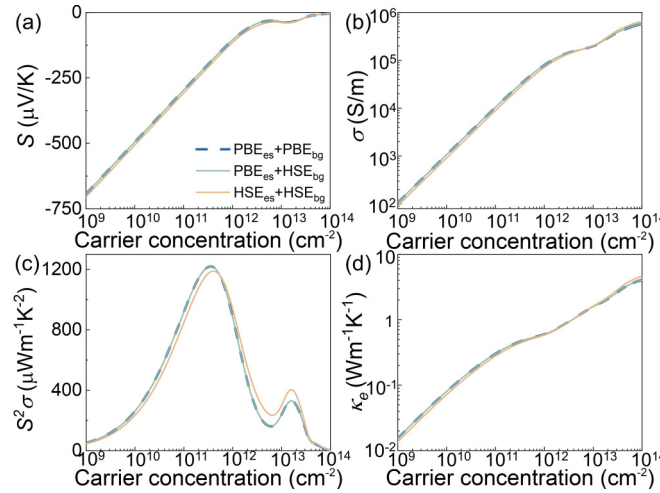

FIG. 12. Calculated room-temperature Seebeck coefficient, electrical conductivity, power factor, and electrical thermal conductivity as a function of carrier concentration.

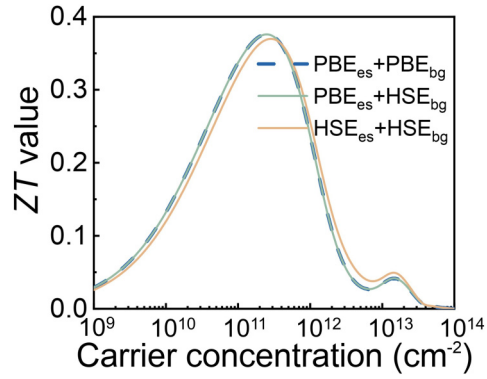

FIG. 13. Calculated room-temperature *ZT* value as a function of carrier concentration.

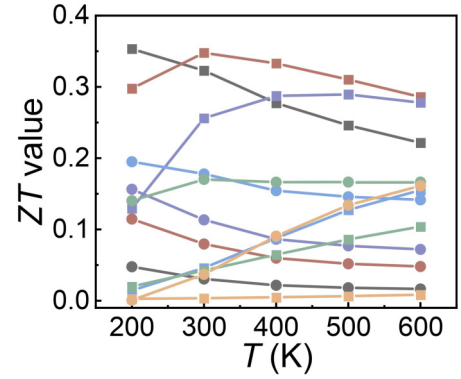

FIG. 15. Calculated *ZT* value at certain different temperatures and carrier concentrations.

structures, while applying a scissor operator to the conduction bands, such that the band gap is the same as that from the HSE (denoted as PBEes+HSEbg); and (3) start from the HSE-calculated band structures and band gap (denoted as HSEes+HSEbg). Figure 11 shows the calculated room-temperature electron-phonon scattering rates, where the CBM has been shifted to 0 eV. It is found that the scattering rates from methods 1 and 2 are the same. This finding implies that only the change in band gap would not affect the electron-phonon scattering rates.

This can be understood from Eq. (2). For convenience, we rewrite Eq. (2) as

$$\frac{1}{\tau_{i\mathbf{k}}} = \frac{2\pi}{\hbar}\sum_{j,i'}\int_{\mathrm{BZ}}\frac{d\mathbf{q}}{\Omega_{\mathrm{BZ}}}\left|g(i\mathbf{k}, i'\mathbf{k}', j\mathbf{q})\right|^2 C_{i\mathbf{k},i'\mathbf{k}',j\mathbf{q}}\frac{1-f_{i'\mathbf{k}'}}{1-f_{i\mathbf{k}}}, \tag{A3}$$

where

$$C_{i\mathbf{k},i'\mathbf{k}',j\mathbf{q}} = n_{j\mathbf{q}}\delta(E_{i\mathbf{k}} - E_{i'\mathbf{k}'} + \hbar\omega_{j\mathbf{q}})\delta_{\mathbf{k}+\mathbf{q},\mathbf{k}'+\mathbf{G}} + (1+n_{j\mathbf{q}})\delta(E_{i\mathbf{k}} - E_{i'\mathbf{k}'} - \hbar\omega_{j\mathbf{q}})\delta_{\mathbf{k}-\mathbf{q},\mathbf{k}'+\mathbf{G}}. \tag{A4}$$

$C_{i\mathbf{k},i'\mathbf{k}',j\mathbf{q}}$ is the number of phonons capable of scattering the initial electron state $i\mathbf{k}$ into the infinitesimal energy window around the final electron state $i'\mathbf{k}'$, divided by the range of the energy window. For semiconductors, the electron scattering rates are the summation of transition rates between conduction band electronic states, while the hole scattering rates are the summation of transition rates between valence band electronic states. The transition rates between conduction band electronic states and valence band electronic states are negligible. Therefore, $C_{i\mathbf{k},i'\mathbf{k}',j\mathbf{q}}$ is independent of the exact value of the band gap. The other term, $\frac{1-f_{i'\mathbf{k}'}}{1-f_{i\mathbf{k}}}$, can be written as

$$\frac{1-f_{i'\mathbf{k}'}}{1-f_{i\mathbf{k}}} = \frac{1-\frac{1}{e^{(E_{i'\mathbf{k}'}-E_f)/k_BT}+1}}{1-\frac{1}{e^{(E_{i\mathbf{k}}-E_f)/k_BT}+1}} = \frac{e^{(E_{i\mathbf{k}}-E_f)/k_BT}+1}{e^{(E_{i'\mathbf{k}'}-E_f)/k_BT}+1}\cdot e^{(E_{i'\mathbf{k}'}-E_{i\mathbf{k}})/k_BT}. \tag{A5}$$

Hence, $\frac{1-f_{i'\mathbf{k}'}}{1-f_{i\mathbf{k}}}$ is mainly determined by $e^{(E_{i'\mathbf{k}'}-E_{i\mathbf{k}})/k_BT}$ (which is independent of the exact value of the band gap). However, not only the band gap but the band shape is also altered with HSE. This is reflected in the electron-phonon scattering rates shown in Fig. 11.

Figures 11(b), 12, and 13 show the calculated room-temperature electron mobility, and thermoelectric transport

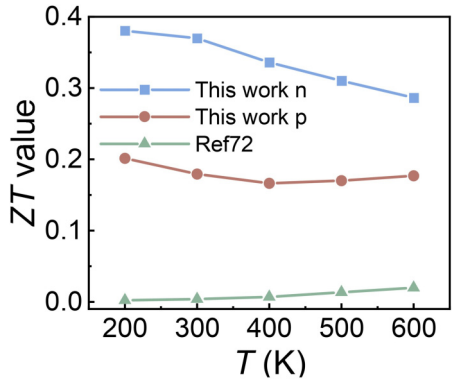

FIG. 14. Calculated maximum *ZT* values at various temperatures. The result from Ref. [72] (*n* type) is shown as a comparison.

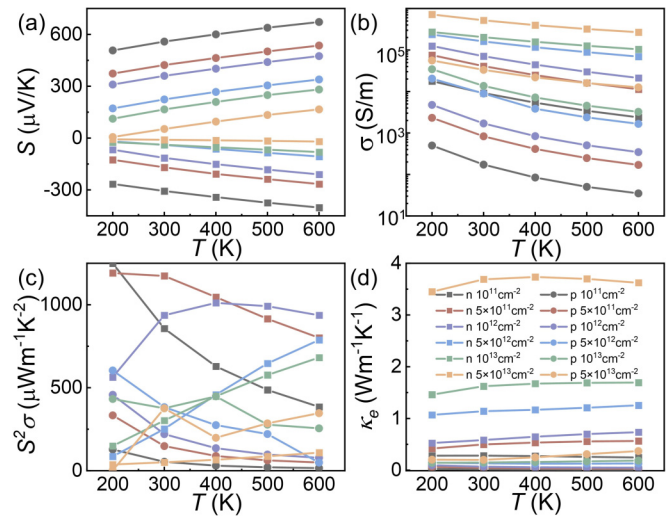

FIG. 16. The corresponding Seebeck coefficient, electrical conductivity, power factor, and electrical thermal conductivity at certain different temperatures and carrier concentrations.

coefficients at various carrier concentrations within the three methods. It is found that the transport coefficients are the same at a certain carrier concentration for methods 1 and 2, which is consistent with the above discussions of the electron-phonon scattering rates.

APPENDIX D: CALCULATED MAXIMUM *ZT* VALUES AT VARIOUS TEMPERATURES

Figure 14 shows the calculated maximum *ZT* values at various temperatures. The results from Ref. [72] (*n* type) are shown as a comparison. It is found that the calculated maximum *ZT* values in Ref. [72] are much lower than our results, which is because of the much smaller relaxation time predicted in Ref. [72]. We observe that the authors stated, "Our computed value of τ for μ near the bottom of the CB" in Ref. [72]. Therefore, we suppose that their constant relaxation time is extracted from the conduction band minimum (CBM). In general, the scattering rate of the CBM is smaller than higher energy states, because there is only absorption process for the CBM state (which is restricted by the energy conservation law; the CBM state cannot emit a phonon and transit to a lower energy state). We are not sure why the τ in Ref. [72] is so small. Moreover, the maximum *ZT* value increases with increasing temperature in Ref. [72]. Nevertheless, we would like to emphasize the importance of the variation of scattering rates in different electronic states in predicting the thermoelectric transport coefficients and the trends with temperature.

APPENDIX E: THE *ZT* VALUES AND CORRESPONDING THERMOELECTRIC TRANSPORT COEFFICIENTS AT DIFFERENT TEMPERATURES AND CARRIER CONCENTRATIONS

Figures 15 and 16 show the variation of calculated ZT values and the corresponding Seebeck coefficient, electrical conductivity, power factor and electrical thermal conductivity at different temperatures at certain carrier concentrations. Here, we have considered six carrier concentrations ranging from 10^{11} cm^{-2} to 5×10^{13} cm^{-2}.

[1] J. He and T. M. Tritt, Advances in thermoelectric materials research: Looking back and moving forward, Science **357**, eaak9997 (2017).

[2] G. J. Snyder and E. S. Toberer, Complex thermoelectric materials, Nat. Mater. **7**, 105 (2008).

[3] G. Tan, L.-D. Zhao, and M. G. Kanatzidis, Rationally designing high-performance bulk thermoelectric materials, Chem. Rev. **116**, 12123 (2016).

[4] B. C. Sales, D. Mandrus, and R. K. Williams, Filled skutterudite antimonides: A new class of thermoelectric materials, Science **272**, 1325 (1996).

[5] H. S. Kim, W. Liu, G. Chen, C.-W. Chu, and Z. Ren, Relationship between thermoelectric figure of merit and energy conversion efficiency, Proc. Natl. Acad. Sci. USA **112**, 8205 (2015).

[6] H. J. Goldsmid and R. W. Douglas, The use of semiconductors in thermoelectric refrigeration, Br. J. Appl. Phys. **5**, 386 (1954).

[7] Y. Pei, X. Shi, A. LaLonde, H. Wang, L. Chen, and G. J. Snyder, Convergence of electronic bands for high performance bulk thermoelectrics, Nature (London) **473**, 66 (2011).

[8] K. Biswas, J. He, I. D. Blum, I. Chun, T. P. Hogan, D. N. Seidman, V. P. Dravid, and M. G. Kanatzidis, Correction: Corrigendum: High-performance bulk thermoelectrics with all-scale hierarchical architectures, Nature (London) **490**, 570 (2012).

[9] B. Jiang, Y. Yu, J. Cui, X. Liu, L. Xie, J. Liao, Q. Zhang, Y. Huang, S. Ning, B. Jia *et al.*, High-entropy-stabilized chalcogenides with high thermoelectric performance, Science **371**, 830 (2021).

[10] L.-D. Zhao, G. Tan, S. Hao, J. He, Y. Pei, H. Chi, H. Wang, S. Gong, H. Xu, V. P. Dravid *et al.*, Ultrahigh power factor and thermoelectric performance in hole-doped single-crystal SnSe, Science **351**, 141 (2016).

[11] K. Biswas, J. He, I. D. Blum, C.-I. Wu, T. P. Hogan, D. N. Seidman, V. P. Dravid, and M. G. Kanatzidis, High-performance bulk thermoelectrics with all-scale hierarchical architectures, Nature (London) **489**, 414 (2012).

[12] X. Li, Y. Lou, K. Jin, L. Fu, P. Xu, Z. Shi, T. Feng, and B. Xu, Realizing zT>2 in environment-friendly monoclinic Cu_2S−tetragonal $Cu_{1.96}S$ nano-phase junctions for thermoelectrics, Angew. Chem. Int. Ed. **61**, e202212885 (2022).

[13] L. D. Hicks and M. S. Dresselhaus, Effect of quantum-well structures on the thermoelectric figure of merit, Phys. Rev. B **47**, 12727 (1993).

[14] L. D. Hicks and M. S. Dresselhaus, Thermoelectric figure of merit of a one-dimensional conductor, Phys. Rev. B **47**, 16631 (1993).

[15] M.-J. Lee, J.-H. Ahn, J. H. Sung, H. Heo, S. G. Jeon, W. Lee, J. Y. Song, K.-H. Hong, B. Choi, S.-H. Lee *et al.*, Thermoelectric materials by using two-dimensional materials with negative correlation between electrical and thermal conductivity, Nat. Commun. **7**, 12011 (2016).

[16] Y. Zhang, B. Feng, H. Hayashi, C.-P. Chang, Y.-M. Sheu, I. Tanaka, Y. Ikuhara, and H. Ohta, Double thermoelectric power factor of a 2D electron system, Nat. Commun. **9**, 2224 (2018).

[17] D. Li, Y. Gong, Y. Chen, J. Lin, Q. Khan, Y. Zhang, Y. Li, H. Zhang, and H. Xie, Recent progress of two-dimensional thermoelectric materials, Nano Micro Lett. **12**, 36 (2020).

[18] K. Kaur, S. A. Khandy, S. Dhiman, U. B. Sharopov, and J. Singh, Computational prediction of thermoelectric properties of 2D materials, Electron. Struct. **4**, 023001 (2022).

[19] P. Z. Jia, J. P. Xie, X. K. Chen, Y. Zhang, X. Yu, Y. J. Zeng, Z. X. Xie, Y. X. Deng, and W. X. Zhou, Recent progress of two-dimensional heterostructures for thermoelectric applications, J. Phys. Condens. Matter **35**, 073001 (2022).

[20] X. Yang, D. Han, M. Wang, M. Du, and X. Wang, Extraordinary thermoelectric performance in 2D group III monolayer XP_3 (X = Al, Ga, and In), J. Phys. D Appl. Phys. **54**, 435501 (2021).

[21] S. Zhang, X. Niu, Y. Xie, K. Gong, H. Shao, Y. Hu, and Y. Wang, High intrinsic ZT in InP_3 monolayer at room temperature, J. Phys.: Condens. Matter **31**, 365501 (2019).

[22] L. Cheng and C. Li, Searching for high-performance two-dimensional channel materials from first-principles calculations, J. Phys. Chem. C **126**, 21149 (2022).

[23] T. Ouyang, E. Jiang, C. Tang, J. Li, C. He, and J. Zhong, Thermal and thermoelectric properties of monolayer indium triphosphide (InP_3): A first-principles study, J. Mater. Chem. A **6**, 21532 (2018).

[24] Z. Sun, K. Yuan, Z. Chang, S. Bi, X. Zhang, and D. Tang, Ultra-low thermal conductivity and high thermoelectric performance of two-dimensional triphosphides (InP_3, GaP_3, SbP_3 and SnP_3): A comprehensive first-principles study, Nanoscale **12**, 3330 (2020).

[25] W. Li, J. Carrete, N. A. Katcho, and N. Mingo, ShengBTE: A solver of the Boltzmann transport equation for phonons, Comput. Phys. Commun. **185**, 1747 (2014).

[26] A. Togo, L. Chaput, and I. Tanaka, Distributions of phonon lifetimes in Brillouin zones, Phys. Rev. B **91**, 094306 (2015).

[27] A. Togo, L. Chaput, T. Tadano, and I. Tanaka, Implementation strategies in phonopy and phono3py, J. Phys. Condens. Matter **35**, 353001 (2023).

[28] T. Tadano, Y. Gohda, and S. Tsuneyuki, Anharmonic force constants extracted from first-principles molecular dynamics: Applications to heat transfer simulations, J. Phys.: Condens. Matter **26**, 225402 (2014).

[29] B. Zhang, Z. Fan, C. Y. Zhao, and X. Gu, GPU_PBTE: An efficient solver for three and four phonon scattering rates on graphics processing units, J. Phys.: Condens. Matter **33**, 495901 (2021).

[30] A. Cepellotti, J. Coulter, A. Johansson, N. S. Fedorova, and B. Kozinsky, Phoebe: A high-performance framework for solving phonon and electron Boltzmann transport equations, J. Phys. Mater. **5**, 035003 (2022).

[31] G. K. H. Madsen and D. J. Singh, BoltzTraP. A code for calculating band-structure dependent quantities, Comput. Phys. Commun. **175**, 67 (2006).

[32] G. K. H. Madsen, J. Carrete, and M. J. Verstraete, BoltzTraP2, a program for interpolating band structures and calculating semi-classical transport coefficients, Comput. Phys. Commun. **231**, 140 (2018).

[33] J. Bardeen and W. Shockley, Deformation potentials and mobilities in non-polar crystals, Phys. Rev. **80**, 72 (1950).

[34] J. Xi, M. Long, L. Tang, D. Wang, and Z. Shuai, First-principles prediction of charge mobility in carbon and organic nanomaterials, Nanoscale **4**, 4348 (2012).

[35] C. Gayner and K. K. Kar, Recent advances in thermoelectric materials, Prog. Mater Sci. **83**, 330 (2016).

[36] L. Cheng and Y. Liu, What limits the intrinsic mobility of electrons and holes in two dimensional metal dichalcogenides? J. Am. Chem. Soc. **140**, 17895 (2018).

[37] L. Cheng, C. Zhang, and Y. Liu, Why two-dimensional semiconductors generally have low electron mobility, Phys. Rev. Lett. **125**, 177701 (2020).

[38] L. Cheng, C. Zhang, and Y. Liu, Intrinsic charge carrier mobility of 2D semiconductors, Comput. Mater. Sci. **194**, 110468 (2021).

[39] V.-A. Ha, B. Karasulu, R. Maezono, G. Brunin, J. B. Varley, G.-M. Rignanese, B. Monserrat, and G. Hautier, Boron phosphide as a *p*-type transparent conductor: Optical absorption and transport through electron-phonon coupling, Phys. Rev. Mater. **4**, 065401 (2020).

[40] R. Biele and R. D'Agosta, Transport coefficients of layered TiS_3, Phys. Rev. Mater. **6**, 014004 (2022).

[41] A. Wang, S. Li, X. Zhang, and H. Bao, Roles of electrons on the thermal transport of 2D metallic MXenes, Phys. Rev. Mater. **6**, 014009 (2022).

[42] W. Li, Electrical transport limited by electron-phonon coupling from Boltzmann transport equation: An *ab initio* study of Si, Al, and MoS_2, Phys. Rev. B **92**, 075405 (2015).

[43] F. Murphy-Armando, Enhancement of the electronic thermoelectric properties of bulk strained silicon-germanium alloys using the scattering relaxation times from first-principles calculations, J. Appl. Phys. **126**, 215103 (2019).

[44] M. Fiorentini and N. Bonini, Thermoelectric coefficients of *n*-doped silicon from first principles via the solution of the Boltzmann transport equation, Phys. Rev. B **94**, 085204 (2016).

[45] J.-J. Zhou, J. Park, I. T. Lu, I. Maliyov, X. Tong, and M. Bernardi, Perturbo: A software package for *ab initio* electron–phonon interactions, charge transport and ultrafast dynamics, Comput. Phys. Commun. **264**, 107970 (2021).

[46] S. Poncé, Y. Gillet, J. Laflamme Janssen, A. Marini, M. Verstraete, and X. Gonze, Temperature dependence of the electronic structure of semiconductors and insulators, J. Chem. Phys. **143**, 102813 (2015).

[47] G. Kresse and J. Hafner, *Ab initio* molecular dynamics for liquid metals, Phys. Rev. B **47**, 558 (1993).

[48] G. Kresse and J. Hafner, *Ab initio* molecular-dynamics simulation of the liquid-metal-amorphous-semiconductor transition in germanium, Phys. Rev. B **49**, 14251 (1994).

[49] G. Kresse and J. Furthmüller, Efficiency of *ab-initio* total energy calculations for metals and semiconductors using a plane-wave basis set, Comput. Mater. Sci. **6**, 15 (1996).

[50] A. Togo, First-principles phonon calculations with phonopy and phono3py, J. Phys. Soc. Jpn. **92**, 012001 (2022).

[51] M. Omini and A. Sparavigna, An iterative approach to the phonon Boltzmann equation in the theory of thermal conductivity, Physica B **212**, 101 (1995).

[52] P. Giannozzi, S. Baroni, N. Bonini, M. Calandra, R. Car, C. Cavazzoni, D. Ceresoli, G. L. Chiarotti, M. Cococcioni, I. Dabo *et al.*, QUANTUM ESPRESSO: A modular and open-source software project for quantum simulations of materials, J. Phys.: Condens. Matter **21**, 395502 (2009).

[53] D. R. Hamann, Optimized norm-conserving Vanderbilt pseudopotentials, Phys. Rev. B **88**, 085117 (2013).

[54] M. Schlipf and F. Gygi, Optimization algorithm for the generation of ONCV pseudopotentials, Comput. Phys. Commun. **196**, 36 (2015).

[55] J. P. Perdew, K. Burke, and M. Ernzerhof, Generalized gradient approximation made simple, Phys. Rev. Lett. **77**, 3865 (1996).

[56] J. Heyd, G. E. Scuseria, and M. Ernzerhof, Hybrid functionals based on a screened Coulomb potential, J. Chem. Phys. **118**, 8207 (2003).

[57] J. M. Ziman, *Electrons and Phonons: The Theory of Transport Phenomena in Solids* (Oxford University Press, Oxford, UK, 2001).

[58] S. Baroni, S. de Gironcoli, A. Dal Corso, and P. Giannozzi, Phonons and related crystal properties from density functional perturbation theory, Rev. Mod. Phys. **73**, 515 (2001).

[59] F. Giustino, Electron-phonon interactions from first principles, Rev. Mod. Phys. **89**, 015003 (2017).

[60] A. A. Mostofi, J. R. Yates, Y.-S. Lee, I. Souza, D. Vanderbilt, and N. Marzari, wannier90: A tool for obtaining maximally localised Wannier functions, Comput. Phys. Commun. **178**, 685 (2008).

[61] S. Poncé, E. R. Margine, C. Verdi, and F. Giustino, EPW: Electron–phonon coupling, transport and superconducting properties using maximally localized Wannier functions, Comput. Phys. Commun. **209**, 116 (2016).

[62] T. Sohier, M. Calandra, and F. Mauri, Two-dimensional Fröhlich interaction in transition-metal dichalcogenide monolayers: Theoretical modeling and first-principles calculations, Phys. Rev. B **94**, 085415 (2016).

[63] G. Chen, *Nanoscale Energy Transport and Conversion: A Parallel Treatment of Electrons, Molecules, Phonons, and Photons* (Oxford University Press, Oxford, UK, 2005).

[64] K. Momma and F. Izumi, VESTA 3 for three-dimensional visualization of crystal, volumetric and morphology data, J. Appl. Crystallogr. **44**, 1272 (2011).

[65] H. Euchner, S. Pailhès, L. T. K. Nguyen, W. Assmus, F. Ritter, A. Haghighirad, Y. Grin, S. Paschen, and M. de Boissieu, Phononic filter effect of rattling phonons in the thermoelectric clathrate $Ba_8Ge_{40+x}Ni_{6-x}$, Phys. Rev. B **86**, 224303 (2012).

[66] S. Pailhès, H. Euchner, V. M. Giordano, R. Debord, A. Assy, S. Gomès, A. Bosak, D. Machon, S. Paschen, and M. de Boissieu, Localization of propagative phonons in a perfectly crystalline solid, Phys. Rev. Lett. **113**, 025506 (2014).

[67] H.-J. Pang, L.-C. Chen, H. Yu, P.-F. Qiu, G.-H. Zhong, Q. Peng, and X.-J. Chen, Hybridization-driven strong anharmonicity in Yb-filled skutterudites, Phys. Rev. B **105**, 094115 (2022).

[68] W. Li and N. Mingo, Ultralow lattice thermal conductivity of the fully filled skutterudite $YbFe_4Sb_{12}$ due to the flat avoided-crossing filler modes, Phys. Rev. B **91**, 144304 (2015).

[69] D. L. Nika and A. A. Balandin, Phonons and thermal transport in graphene and graphene-based materials, Rep. Prog. Phys. **80**, 036502 (2017).

[70] A. Jain and A. J. H. McGaughey, Strongly anisotropic in-plane thermal transport in single-layer black phosphorene, Sci. Rep. **5**, 8501 (2015).

[71] X. Gu and R. Yang, Phonon transport in single-layer transition metal dichalcogenides: A first-principles study, Appl. Phys. Lett. **105**, 131903 (2014).

[72] S. P. Keshri and A. Medhi, Enhanced thermoelectric efficiency of monolayer InP_3 under strain: A first-principles study, J. Phys. Condens. Matter **33** 225701 (2021).

[73] B. Smith, B. Vermeersch, J. Carrete, E. Ou, J. Kim, N. Mingo, D. Akinwande, and L. Shi, Temperature and thickness dependences of the anisotropic in-plane thermal conductivity of black phosphorus, Adv. Mater. **29**, 1603756 (2017).

[74] X. Gu, Y. Wei, X. Yin, B. Li, and R. Yang, Colloquium: Phononic thermal properties of two-dimensional materials, Rev. Mod. Phys. **90**, 041002 (2018).

[75] L. Cheng, C. Zhang, and Y. Liu, The optimal electronic structure for high-mobility 2D semiconductors: Exceptionally high hole mobility in 2D antimony, J. Am. Chem. Soc. **141**, 16296 (2019).

[76] T. Sohier, D. Campi, N. Marzari, and M. Gibertini, Mobility of two-dimensional materials from first principles in an accurate and automated framework, Phys. Rev. Mater. **2**, 114010 (2018).

[77] B. Liao, J. Zhou, B. Qiu, M. S. Dresselhaus, and G. Chen, *Ab initio* study of electron-phonon interaction in phosphorene, Phys. Rev. B **91**, 235419 (2015).

[78] G. Du, C. Li, and L. Cheng, Origin of contrasting trends of intrinsic electron mobility with tensile strain in hexagonal MoS_2 and triangular $PdSe_2$, Phys. Rev. B **107**, 085422 (2023).

[79] O. Hellman, P. Steneteg, I. A. Abrikosov, and S. I. Simak, Temperature dependent effective potential method for accurate free energy calculations of solids, Phys. Rev. B **87**, 104111 (2013).

[80] G. Qin and M. Hu, Accelerating evaluation of converged lattice thermal conductivity, npj Comput. Mater. **4**, 3 (2018).